



Modulating electronic structure and sulfur p-band center by anchoring amorphous Ni@NiS_x on crystalline CdS for expediting photocatalytic H₂ evolution

Xinlei Zhang^a, Fei Wu^a, Guicun Li^a, Lei Wang^b, Jianfeng Huang^c, Alan Meng^{b,*}, Zhenjiang Li^{a,*}

^a College of Materials Science and Engineering, Qingdao University of Science and Technology, Qingdao, Shandong 266042, PR China

^b Key Laboratory of Optic-electric Sensing and Analytical Chemistry for Life Science, College of Chemistry and Molecular Engineering, Qingdao University of Science and Technology, Qingdao, Shandong 266042, PR China

^c School of Material Science and Engineering, Xi'an Key Laboratory of Green Manufacture of Ceramic Materials, Shaanxi University of Science and Technology, Xi'an, Shaanxi 710021, PR China

ARTICLE INFO

Keywords:

Partial reduction strategy
CdS nanorod
P-band center
Charge extraction ability
Photocatalytic H₂ production

ABSTRACT

Photocatalytic water splitting is a prospective approach to address the energy and environmental challenges. Herein, an amorphous Ni@NiS_x cocatalyst has been fabricated and simultaneously assembled onto CdS to form amorphous-crystalline Ni@NiS_x-CdS photocatalyst via a partial reduction strategy. Comprehensive experiments and theoretical calculations demonstrate that the synergistic effects between the electronic coupling of amorphous-crystalline interface and the gradient work function variation induced by Ni nanocluster encapsulation achieve the deeper downshift of the S p-band center to optimize H⁺ intermediate adsorption, enhance charge extraction ability through Schottky junction and lower H⁺ adsorption Gibbs free energy (ΔG_{H^+}). Accordingly, the optimal Ni@NiS_x-CdS photocatalyst delivers a remarkable photocatalytic H₂ production rate of 78.7 mmol·g⁻¹·h⁻¹ with an apparent quantum efficiency (AQE) of 36.74% at 420 nm, which is approximately 18.3 and 1.5 times than that of CdS and NiS_x-CdS, respectively. This work offers a novel insight into the development of amorphous nanocomposite cocatalysts for promoting solar-to-H₂ energy conversion.

1. Introduction

Converting renewable solar energy into green hydrogen (H₂) is deemed to be an efficient and promising energy conversion strategy to address the energy depletion crisis and environmental pollution issues [1–4]. Nevertheless, the vast majority of individual host photocatalysts exhibits the finite photocatalytic solar-H₂ conversion efficiency due to the high recombination rate of photogenerated electron-hole pairs, the deficiency and low-activity of the active sites [5–8]. To address these problems, various approaches have been employed to further enhance the photocatalytic H₂ production efficiency, such as semiconductor heterojunction construction [9–12], cocatalyst modification [13–15], and morphology modulation [16,17]. As is well known, cocatalyst modification has been proven to be an effective approach, which can improve the migration and separation efficiency of photogenerated carriers, reduce reaction barrier and activate protons to promote H₂

conversion [18–20]. So far, noble metals (including Pt, Au, Ag and Pd) are widely utilized as outstanding cocatalysts of host photocatalysts for boosting photocatalytic H₂ evolution performance owing to its superior conductivity for charge migration and near-zero Gibbs free energy (ΔG_{H^+}) for interfacial H₂ evolution [21–25]. Unfortunately, the high cost and low abundance of noble metal-based cocatalysts still remains the main bottleneck to restrict large-scale practical usage in the future. Therefore, it is the potential long-term significance to develop earth-abundance, cost-effective and highly-active cocatalysts with the aim of boosting photocatalytic H₂ evolution performance.

Transition metal chalcogenides, in particular nickel sulfides (NiS), holds great potential to emerge as an ideal substitute to the Pt-group metals owing to the low overpotentials, abundant active sites, and cost-effectiveness [26–28]. Based on the previous report, the exposed S atoms at the edge of crystalline NiS can serve as photocatalytic active sites, which can effectively capture protons in solution for

* Corresponding authors.

E-mail addresses: alanmengqust@163.com (A. Meng), zhenjiangli@qust.edu.cn (Z. Li).

<https://doi.org/10.1016/j.apcatb.2023.123398>

Received 25 July 2023; Received in revised form 1 October 2023; Accepted 14 October 2023

Available online 17 October 2023

0926-3373/© 2023 Elsevier B.V. All rights reserved.

photocatalytic H_2 production [29–31]. However, conventional crystalline NiS cocatalysts expose insufficient amount of active S sites to participate in the photocatalytic reaction due to their regular structure, large particle size and ordered lattice arrangement, which hinders the improvement of photocatalytic H_2 evolution activity [31–33]. Notably, the intrinsic disorderliness of amorphous NiS_x can create abundant “dangling bonds” in the loose atomic free-volume unit, which can rationally break the periodicity of the crystal structures, thereby providing more active S sites. In addition to enriching the S sites in the cocatalyst, another critical prerequisite for designing efficient sulfide photocatalysts is to regulate the appropriate S-H binding energy for the fast H_2 desorption. For metal sulfides (NiS_x [34], MoS_x [35], CdS [36], etc.), the adsorption interaction between the p orbitals of active S site and s orbitals of H^* intermediate is hybridized, which lead to fully occupied bonding orbital at the low energy level and partially occupied antibonding orbital at the high energy level. Unfortunately, the S site presents a strong bonding with adsorbed H^* intermediate due to its less antibonding states occupancy, which is unfavorable to subsequent H_2 desorption [35,37,38]. Therefore, weakening the S- H^* intermediate binding energy and balancing adsorption/desorption behavior of H^* intermediate is considered as an effective strategy through tuning the electronic structure configuration and charge redistribution of active S sites [39,40]. Currently, the p-band center (ϵ_p) to Fermi level were considered to be valid descriptors to reflect the H^* intermediates' adsorption behaviors, with the movement of p-band center away from (close to) the Fermi level resulting in more (less) antibonding states occupancy, corresponding to weaker (stronger) bonding with active S sites. Hence, regulating p-band center is expected to be the intuitive design criterion for the efficient sulfide photocatalysts.

The amorphous-crystalline interfacial engineering between the cocatalyst and the host-catalyst facilitates the interfacial charge transfer, which can realize the p-band center regulation of active sites in composite photocatalyst [41,42]. Meanwhile, on this basis, if the chemical bond is built at the amorphous-crystal interface as an electron “bridge”, the charge transfer efficiency between the cocatalyst and the host-catalyst can be significantly improved due to the lowered charge transfer energy barrier [43]. In addition, in order to improve the charge transport efficiency of amorphous material, embedding ultra-small nanoclusters into amorphous materials is an effective strategy [44,45]. The encapsulation of nanoclusters with superior electrical conductivity into amorphous materials would not only facilitate the charge separation and transfer kinetics, but also be conducive to regulating the p-band center of active sites to balance adsorption/desorption behavior of H^* intermediate. Regrettably, the work about enriching active sites and tailoring p-band center for efficient photocatalytic performance based on constructing the amorphous Ni@NiS_x cocatalyst modified CdS has not been reported.

In this work, an amorphous Ni@NiS_x cocatalyst was constructed on the CdS to synthesize amorphous-crystalline $\text{Ni@NiS}_x\text{-CdS}$ photocatalyst with abundant active S sites through a facile partial reduction strategy. Of significance is that the optimal $\text{Ni@NiS}_x\text{-CdS}$ photocatalyst exhibit high H_2 production rate of $78.7 \text{ mmol} \cdot \text{g}^{-1} \cdot \text{h}^{-1}$ accompany by apparent quantum efficiency (AQE) of 36.74% at 420 nm, which is approximately 18.3 and 1.5 times than that of CdS and $\text{NiS}_x\text{-CdS}$, respectively. Both experimental and theoretical results comprehensively indicate that the amorphous-crystalline interfaces with Cd-S-Ni binding bridge and the encapsulation of Ni clusters into amorphous NiS_x realizes the deeply downshift of the S p-band center to optimize the binding interaction between the active S sites and H^* intermediates, drives the activation of H_2O molecules to promote the dissociation of H_2O , and lower H^* adsorption Gibbs free energy (ΔG_{H^*}) to expedite H_2 evolution. Furthermore, the charge extraction efficiency of Ni@NiS_x is strengthened by incorporating Ni clusters due to the gradient work function difference, which effectively suppresses charge recombination. In addition, amorphous NiS_x can expose abundant unsaturated S sites, which is favorable for enriching protons and electrons at the S sites. This

work offers a new avenue to fabricate the highly-efficient sulfide photocatalysts by coupling amorphous nanohybrid cocatalysts with semiconductor for photocatalytic conversion reaction.

2. Experimental section

2.1. Chemicals and materials

Cadmium acetate dihydrate ($\text{Cd}(\text{COOH})_2 \cdot 2 \text{H}_2\text{O}$), thiourea ($\text{CH}_4\text{N}_2\text{S}$), ethylenediamine ($\text{C}_2\text{H}_8\text{N}_2$), nickel(II) nitrate hexahydrate ($\text{Ni}(\text{NO}_3)_2 \cdot 6 \text{H}_2\text{O}$), and sodium borohydride (NaBH_4) were obtained from Sinopharm Co., LTD, and glutathione (GSH) purchased from Aladdin Reagent Co., LTD. All chemical reagents in analytical grade were used without any further purification.

2.2. Synthesis of CdS nanorod

CdS nanorods were synthesized by a typical solvothermal procedure [62]. Briefly, $\text{Cd}(\text{COOH})_2 \cdot 2 \text{H}_2\text{O}$ (1.64 g, 6 mmol) and thiourea (1.4 g, 18 mmol) were mixed in the ethylenediamine (50 mL). After stirring for 15 min, the mixed solution was transferred to a Teflon-lined autoclave, and then reacted at 180°C for 24 h. After cooling down to room temperature, CdS nanorods were obtained by centrifugation and washed several times with deionized water and absolute ethanol to separate out impurities.

2.3. Synthesis of $\text{Ni@NiS}_x\text{-CdS}$ photocatalysts

The $\text{Ni@NiS}_x\text{-CdS}$ heterostructure photocatalyst was fabricated through a facile wet chemistry partial reduction strategy. In order to investigate the effect of Ni@NiS_x wrapping with various quality on the photoactivity of $\text{Ni@NiS}_x\text{-CdS}$, the following experiments were performed. As-prepared CdS nanorods (100 mg) was dispersed in the mixed solvent of 7.5 mL H_2O and 17.5 mL ethanol with sonication for 15 min, different amount of 100 mM $\text{Ni}(\text{NO}_3)_2 \cdot 6 \text{H}_2\text{O}$ (0.5 mL, 1.0 mL, 1.5 mL, 2.0 mL, and 2.5 mL) was added into the suspension. Then, a certain amount of GSH was dispersed in the mixed solution and the molar ratio of GSH to $\text{Ni}(\text{NO}_3)_2 \cdot 6 \text{H}_2\text{O}$ was maintained at 2:1. Finally, NaBH_4 solution (600 μL , 100 mM) was added dropwise and reacted for 3 h to obtain the $\text{Ni@NiS}_x\text{-CdS}$ composites with different weight ratios (3%, 6%, 9%, 12% and 15%) of Ni@NiS_x cocatalysts. The photocatalysts were collected by centrifugation, washed three times with water and ethanol and dried overnight in a vacuum at 60°C . For comparison, $\text{NiS}_x\text{-CdS}$ sample was prepared via the same procedures without adding NaBH_4 .

To investigate the different influence of the content of Ni clusters in the Ni@NiS_x cocatalyst on the photocatalytic H_2 evolution, various molar contents of NaBH_4 were utilized to reduce. CdS nanorods (100 mg) was dispersed in the mixed solvent of 7.5 mL H_2O and 17.5 mL ethanol with sonication, followed by the addition of $\text{Ni}(\text{NO}_3)_2 \cdot 6 \text{H}_2\text{O}$ solution (1.5 mL, 100 mM). Then, GSH (3 mL, 100 mM) was added to the mixed solution. Finally, various molar mass (20 μmol , 40 μmol , 60 μmol , 80 μmol and 100 μmol) of NaBH_4 solution were added dropwise and the reaction was carried out under continuous stirring for 3 h.

2.4. Photocatalytic activity test

In a typical photocatalytic process, 5 mg of photocatalyst was dispersed in 100 mL of aqueous solution containing 0.35 M Na_2S and 0.25 M Na_2SO_3 as the sacrificial agent. Photocatalytic reaction system was evacuated for 15 min and kept at 5°C through the recirculating cooling water system (Beijing Perfectlight Technology Co., Ltd.). The photocatalytic reaction was triggered by a 300 W Xenon lamp equipped with an UV cut-off filter ($\lambda > 420 \text{ nm}$) under continuous stirring. The light power was measured to be about 1.5 W by PLMW2000 photoradiometer, which corresponds to the light intensity of $19.10 \text{ mW}/\text{cm}^2$ (irradiation area: 78.5 cm^2). The produced H_2 content was evaluated gas

chromatography. In addition, to ascertain the apparent quantum efficiency (AQE), the experiments were performed under the same conditions, except that the light source used was a monochromatic xenon lamp with wavelengths of 420, 500 and 550 nm, respectively. The apparent quantum efficiency (AQE) is calculated according the

following equation:

$$AQE(\%) = \frac{\text{number of reached electrons}}{\text{number of incident photons}} \times 100$$

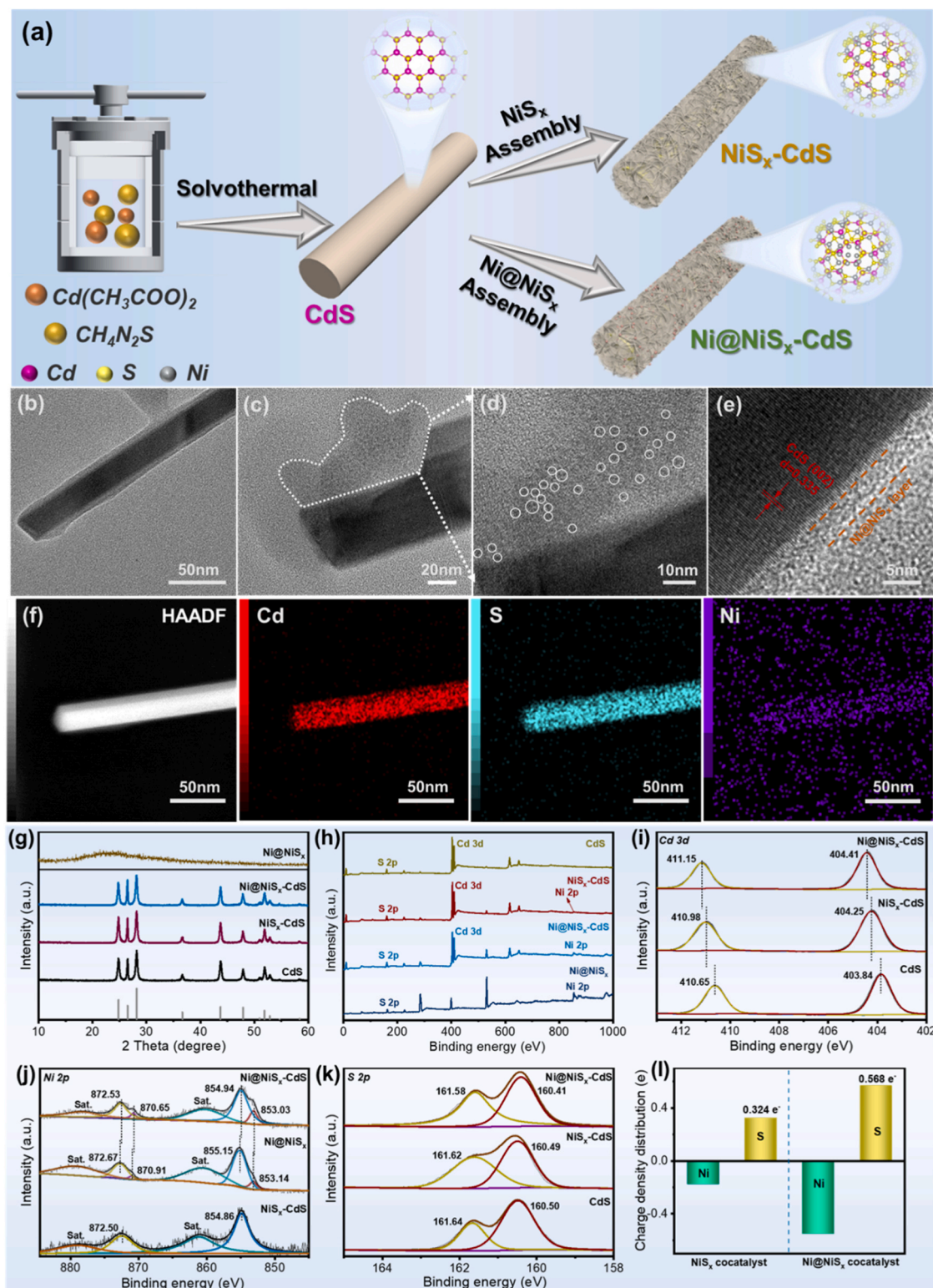


Fig. 1. (a) Schematic of the synthetic process, (b), (c) TEM, (d) magnified TEM of the region outlined in white in (c), (e) HRTEM, (f) corresponding HAADF-STEM and EDS elemental mapping images of coaxial $\text{Ni@NiS}_x\text{-CdS}$ photocatalyst. (g) X-ray diffraction (XRD) patterns and (h) X-ray photoelectron spectroscopy (XPS) survey spectra of pristine CdS, $\text{NiS}_x\text{-CdS}$, $\text{Ni@NiS}_x\text{-CdS}$ and Ni@NiS_x , respectively. High-resolution XPS spectra of (i) Cd 3d (j) Ni 2p and (k) S 2p. (l) The charge density distributions of NiS_x in $\text{NiS}_x\text{-CdS}$ and Ni@NiS_x in $\text{Ni@NiS}_x\text{-CdS}$, respectively.

$$= \frac{\text{number of evolved } H_2 \text{ molecules} \times 2}{\text{number of incident photons}} \times 100$$

$$= \frac{2R_{H_2}t_1N_A}{EAt_2\lambda/hc} \quad (1)$$

Details of the AQE calculation were provided in the [supporting information](#).

3. Results and discussion

3.1. Structural and morphological characterization

The overall synthetic route of amorphous Ni@NiS_x cocatalyst wrapped CdS nanorod are schematically shown in Fig. 1a. CdS nanorod was first synthesized via a simple solvothermal reaction of cadmium acetate with thiourea in ethylenediamine solution. Thereafter, amorphous Ni@NiS_x cocatalyst was successfully assembled onto the CdS surface via a wet-chemistry partial reduction strategy. As shown in Fig. S1, CdS is a typical 1D nanorod with a length and diameter of approximately 0.5–2.0 μm and 30–50 nm, respectively. As clearly shown in the High-resolution TEM (HRTEM) images, the regular lattice spacings of 0.335 nm can be assigned to the (002) plane of hexagonal CdS [46]. Fig. S2 shows TEM images of the coaxial NiS_x-CdS photocatalyst. Amorphous NiS_x is uniformly wrapped on the surface of CdS, and NiS_x-CdS photocatalyst surface becomes much rougher compared to that of the pure CdS. Similar to NiS_x-CdS sample, the desired Ni@NiS_x-CdS photocatalyst with a 1D nanorod is depicted in Fig. 1b. The high magnification image (Fig. 1c and d) clearly shows that plenty of spotted Ni clusters (highlighted by white circles) encapsulated within the amorphous NiS_x layer. Moreover, amorphous regions around the Ni clusters were observed in the high-magnification TEM images, confirming that Ni clusters were encapsulated in the amorphous NiS_x layer. As shown in Fig. 1d, no clear lattice fringe was identified in the vicinity of Ni@NiS_x, evidencing poor crystallinity. The inverse fast Fourier transform (IFFT) images and fast Fourier transform (FFT) patterns of the CdS and Ni@NiS_x-CdS photocatalyst were shown in Fig. S3, respectively. It can be clearly observed that the interplanar distance of 0.335 nm can be assigned to the (002) plane of CdS in the blue region, while the orange area represents the amorphous region of Ni@NiS_x. This verifies the existence of heterogeneous interface coupling between highly crystalline CdS and amorphous Ni@NiS_x, which contributes to the enhancement of structural stability and transfer and separation of photogenerated carriers. HRTEM image (Fig. 1e) clearly displays the interplanar spacings of 0.335 nm, which is consistent with the (002) lattice plane of pristine hexagonal CdS, implying amorphous Ni@NiS_x did not alter the crystal structure of CdS. The as-prepared Ni@NiS_x-CdS was also confirmed by high-angle annular dark field-STEM (HAADF-STEM) images in Fig. 1f. Meanwhile, as can be seen from elemental mapping, the nanorod constituted by the Cd element possesses a diameter of about 23.4 nm, which is smaller than that of the nanorods constructed of Ni (27.1 nm) and S (27.7 nm) elements, illustrating that the amorphous Ni@NiS_x cocatalyst is wrapped around the CdS surface.

The phase structures of the as-synthesized samples were measured by X-ray diffraction (XRD). As presented in Fig. 1g, XRD pattern signifies that the principal diffraction peaks locate at 24.8°, 26.5°, 28.2°, 36.6°, 43.8°, 47.8°, and 51.9° corresponding to (100), (002), (101), (102), (110), (103) and (112) planes of the hexagonal phase CdS (JCPDS 77–2306) [47]. After depositing amorphous Ni@NiS_x cocatalyst on the CdS surface, no obvious NiS_x species peaks were detected in the NiS_x-CdS samples, indicating that NiS_x possess typical amorphous structure. Meanwhile, the diffraction peaks of Ni clusters were not detected, which may be due to that low amount of Ni clusters with poor crystallinity were encapsulated into amorphous NiS_x. Furthermore, the diffraction peak intensity of CdS remained sharp, confirming that the coating of Ni@NiS_x has little influence on the intrinsic structure of CdS.

Additionally, the low-angle broad hump of Ni@NiS_x is mainly ascribed to its amorphous structure, which stems from the fact that the initial Ni clusters and NiS_x seeds did not grow further at room temperature, but remained in an amorphous state.

To deeply investigate the characteristics for the superior photocatalytic activity of Ni@NiS_x cocatalyst wrapping on CdS nanorods, X-ray photoelectron spectroscopy (XPS) is employed to examine the chemical element states in the as-synthesized photocatalysts. The XPS survey spectra (Fig. 1h) shows that Ni@NiS_x-CdS consist of Cd, Ni, S elements, which confirms the successful preparation of Ni@NiS_x-CdS photocatalyst. As shown in Fig. 1i, the Cd 3d is composed of two characteristic peaks located at 403.84 and 410.65 eV, ascribing to Cd 3d_{5/2} and Cd 3d_{3/2} of pristine CdS, respectively [48]. Compared with pristine CdS, the positive shift of the Cd 3d peak can be observed in NiS_x-CdS sample, which indicates the flow of electrons from CdS to amorphous NiS_x. This proves the strong interaction between the interfaces of CdS and amorphous NiS_x. Moreover, Fig. S4 indicates that two peaks at 855.27 and 872.75 eV are ascribed to the binding energies of Ni-S bond, which reduces the energy barrier for charge transfer. Fig. 1j shows that two signal peaks of Ni²⁺ 2p_{3/2} and Ni²⁺ 2p_{1/2} in NiS_x-CdS are located at 854.86 and 872.50 eV, accompanied by two distinct satellite peaks at 862.1 and 880.5 eV, respectively [27,49]. Particularly, the Ni 2p XPS spectra of Ni@NiS_x-CdS sample was not only fitted into two peaks centering at 854.94 and 872.53 eV, assigned to the electron orbits of Ni²⁺ 2p_{3/2} and Ni²⁺ 2p_{1/2}, but also deconvoluted into other two peaks at 853.03 and 870.65 eV belonging to the Ni⁰ 2p spectrum, respectively [50,51]. Theoretically, the higher XPS binding energy is derived from the lower electron density [52]. It is noteworthy that the signal peaks of Ni²⁺ 2p and Ni⁰ 2p of Ni@NiS_x-CdS appear negative shift to lower binding energy than those of Ni@NiS_x, while the peaks of Cd 3d_{5/2} and Cd 3d_{3/2} of Ni@NiS_x-CdS exhibits larger shifts toward higher binding energy than that of NiS_x-CdS, manifesting that more free-electrons are enriched on Ni@NiS_x cocatalyst. As sketched in Fig. 1k, the binding energy of the S 2p in the Ni@NiS_x-CdS photocatalyst significantly shifts to lower values compared to the NiS_x-CdS, strongly confirming the increased electron density of active S sites in the Ni@NiS_x-CdS photocatalyst. The XPS results demonstrate that Ni@NiS_x extracts more photogenerated electrons from CdS, which achieves the formation of electron-rich S sites. To further determine the Ni content in Ni@NiS_x-CdS, ICP-AES was conducted out, and the result was shown in Table S1. After calculation, the Ni content of Ni@NiS_x-CdS determined to be 8.46%, respectively, which was almost consistent with the amount of added raw materials. To quantify the electron variation of the active S site, the average charge density distribution was calculated as shown in Fig. 1l and Table S2. The charge density of the S element in the Ni@NiS_x is increased relative to NiS_x. The electron-rich active S sites can facilitate the desorption of H₂ and favor for the formation of H₂ in the photocatalytic process.

3.2. Photocatalytic H₂ evolution performance

The photocatalytic H₂ evolution performance is assessed with Na₂S and Na₂SO₃ as the hole scavengers under visible light irradiation (λ > 420 nm). As observed in Fig. 2a, the individual CdS photocatalyst showed low photocatalytic H₂ activity with an evolution rate of 4.3 mmol·g⁻¹·h⁻¹, due to the lack of surface photocatalytic active sites. As shown in Fig. S5, the evolution rate of H₂ shows an initially increasing and then decreasing trend as the mass ratio of NiS_x to CdS increases. When the Ni content of NiS_x-CdS was adjusted to 9%, and the optimized NiS_x-CdS exhibited an improved H₂ evolution activity of 51.9 mmol·g⁻¹·h⁻¹, which suggested that the enrichment of active S sites on amorphous NiS_x is an effective strategy to enhance H₂ evolution activity. After being coupled with the Ni@NiS_x cocatalyst, the Ni@NiS_x-CdS photocatalysts exhibit significantly enhanced H₂ evolution activity compared to pristine CdS and NiS_x-CdS. As observed in Fig. 2a, the Ni content of Ni@NiS_x-CdS reached to 9%, the Ni@NiS_x-CdS sample

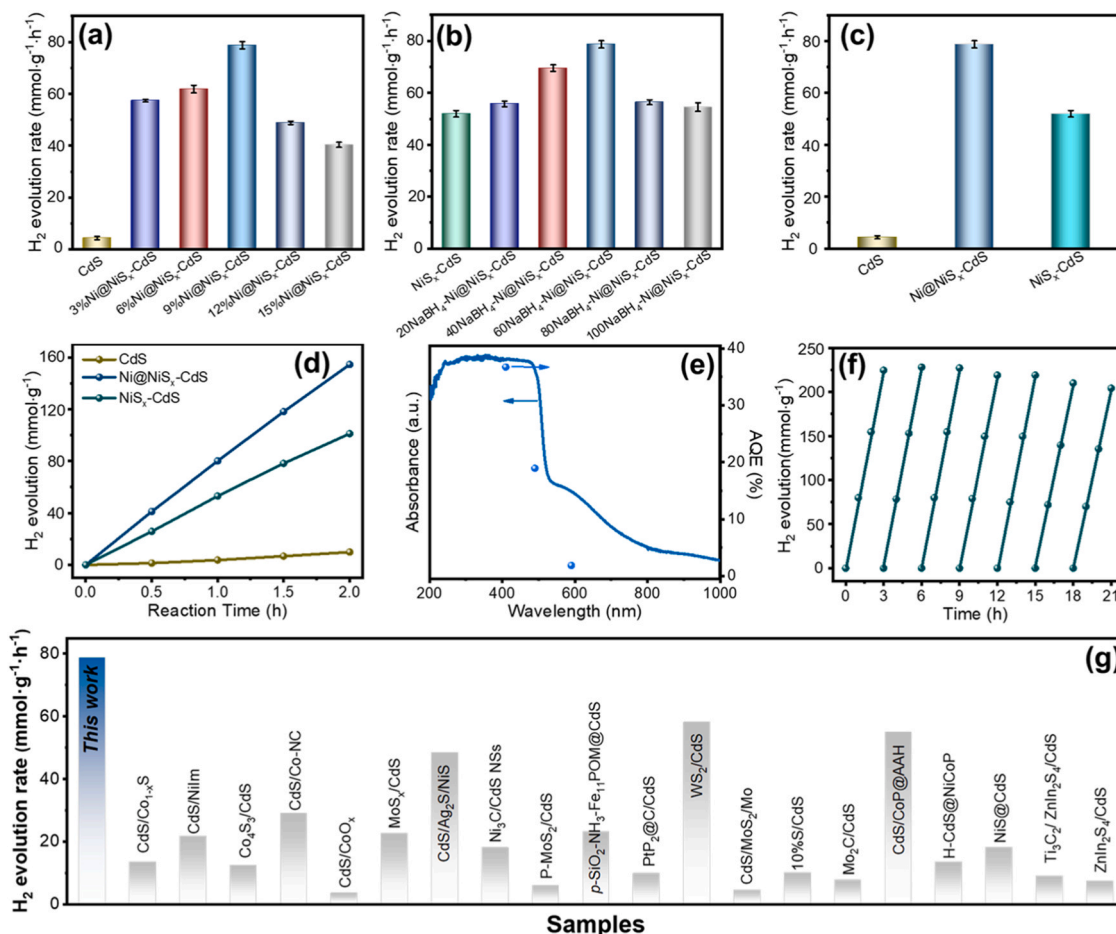


Fig. 2. (a–b) Photocatalytic H₂ evolution rate of different photocatalysts. (c) H₂ evolution rate of different photocatalysts and (d) H₂ evolution amount at different irradiation time. (e) Wavelength-dependent apparent quantum efficiency (AQE). (f) cycling stability test of Ni@NiS_x-CdS. (g) Comparison for H₂ evolution rate with other photocatalysts in recent works.

exhibited the optimal photocatalytic performance with an H₂ production rate of 78.7 mmol·g⁻¹·h⁻¹. To further clarify the essential role of Ni clusters in Ni@NiS_x-CdS cocatalyst on photocatalytic H₂ evolution, various molar content of NaBH₄ was exploited. As shown in Fig. 2b, with the addition of NaBH₄ increasing, the H₂ production rate over Ni@NiS_x-CdS improves. When the addition amount of NaBH₄ was 60 μmol, the actual mass ratio of Ni:NiS_x:CdS was 1.17:14.31:100 (Table S1 and S3), and the optimized Ni@NiS_x-CdS displayed the highest photocatalytic H₂ evolution activity of 78.7 mmol·g⁻¹·h⁻¹, which is approximately 18.3 and 1.5 times higher as compared with pristine CdS photocatalyst and NiS_x-CdS, respectively (Fig. 2c–d). Beyond this point, the excessive Ni clusters and NiS_x emergence could hinder light absorption and act as recombination centers of photogenerated charge carrier, thereby decreasing the photocatalytic performance. Additionally, this optimal result is superior to the H₂ production performance of many reported CdS-based photocatalysts (Fig. 2g and Table S7), which strongly reflects the key role of amorphous Ni@NiS_x cocatalyst on photocatalytic H₂ evolution activity. Furthermore, the apparent quantum efficiency (AQE) of Ni@NiS_x-CdS was measured using different bandpass filters to evaluate the photocatalytic performance in Table S4. As shown in Fig. 2e, the AQE of Ni@NiS_x-CdS reaches a considerable value of 36.74% at 420 nm. Meanwhile, the AQE of photocatalytic H₂ evolution reaction at 500 nm and 600 nm wavelengths corresponds to 18.92% and 1.84%, respectively. It is worth noting that the AQE follows the trend of the UV–vis absorption curve of Ni@NiS_x-CdS, indicating that the H₂ evolution is indeed triggered by the photoexcitation of the photocatalyst. In addition to the photocatalytic apparent quantum efficiency, the recycling

stability of the photocatalysts is pivotal for the practical applications. The photostability of Ni@NiS_x-CdS was carried out to evaluate by long-time cycle test under visible light irradiation as shown in Fig. 2f. The photocatalytic H₂ evolution rate still maintains 91% after seven cycles with each run for 3 h, indicating the superior stability and durability of Ni@NiS_x-CdS photocatalyst. Moreover, the XRD and TEM characterization were carried out to evaluate the photostability of the recycled photocatalyst. The morphology and phase structure of Ni@NiS_x-CdS photocatalyst did not change significantly before and after the reaction (Fig. S6), which further demonstrate the excellent physical and chemical stability of Ni@NiS_x-CdS photocatalyst for H₂ evolution.

3.3. Enhanced photocatalytic performance mechanism

Since the photo-response ability of the photocatalyst plays a key role in the H₂ production performance, the optical absorption properties of as-prepared photocatalysts are recorded by UV–vis absorption spectra. As presented in Fig. 3a, pristine CdS presents a photo-absorption edge at 532 nm, corresponding to its intrinsic band gap. Additionally, the optical absorption was slightly enhanced in the visible region by wrapping NiS_x on the surface of CdS. Noteworthy, Ni@NiS_x-CdS further exhibits the enhanced absorption intensity from visible to near-infrared region due to the superior optical absorption characteristics of Ni@NiS_x, which can advance the utilization of solar energy and favor for visible light-driven photocatalytic H₂ production [53]. To gain insight into the intrinsic mechanism of the enhanced photogenerated carrier separation and migration efficiency of the Ni@NiS_x-CdS, the photoelectrochemical

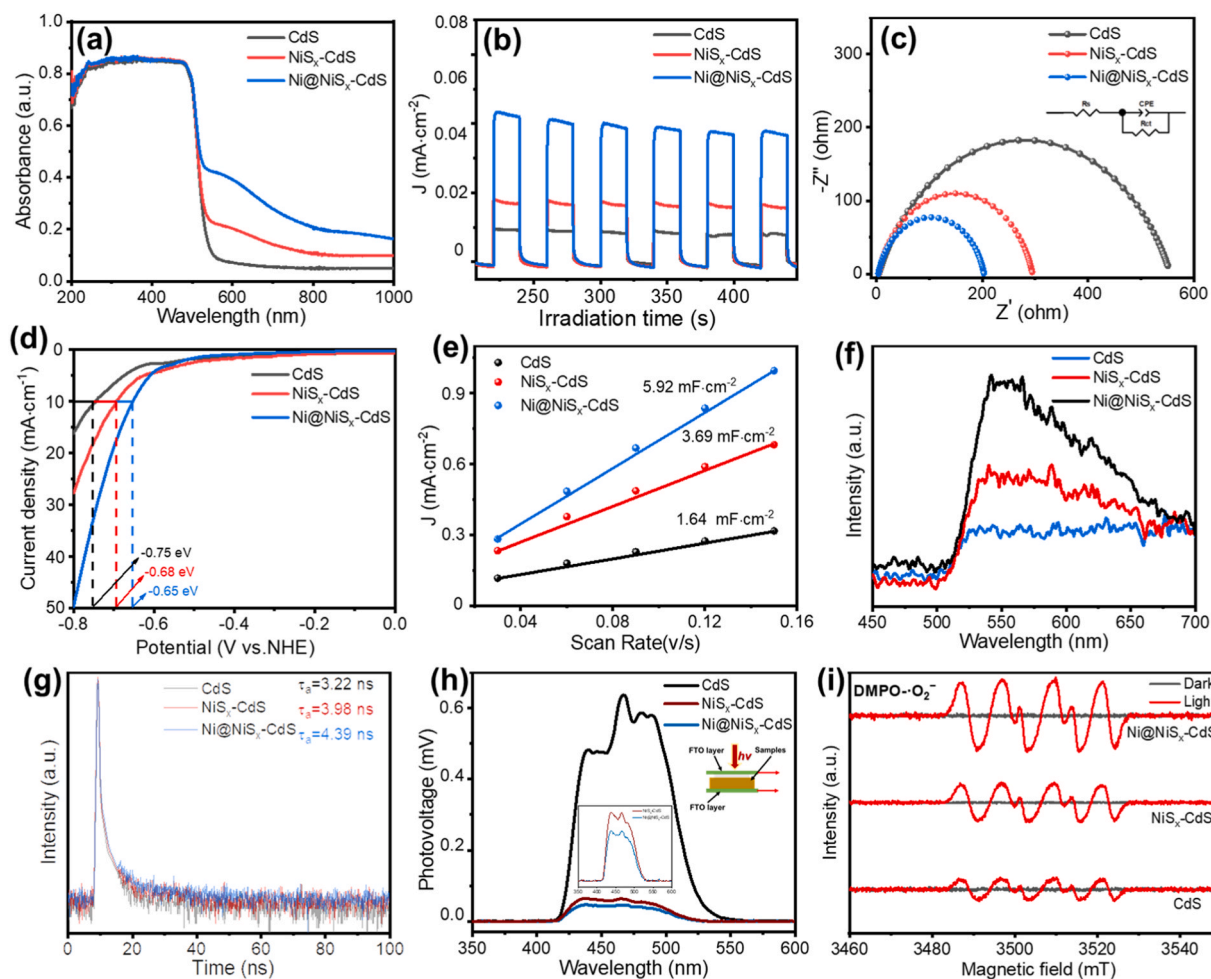


Fig. 3. (a) UV-vis DRS spectra, (b) Transient photocurrent response curves, (c) Electrochemical impedance spectra EIS Nyquist plots, (d) Linear sweep voltammetry LSV curves, (e) Double-layer capacitance (C_{dl}) curves, (f) Steady-state PL spectra, (g) Time-resolved transient PL decay spectra, (h) Steady-state SPV spectra, and (i) ESR spectra of $DMPO-O_2^-$ for CdS, NiS_x -CdS and $Ni@NiS_x$ -CdS.

properties were characterized. Obviously, as displayed in Fig. 3b, the $Ni@NiS_x$ -CdS exhibits the highest current density among as-synthesized photocatalysts, powerfully revealing the effective separation and migration rate of photoinduced electron-hole pairs in $Ni@NiS_x$ -CdS. Electrochemical impedance spectroscopy (EIS) tests were employed to explore charge transport efficiency at the interface of the photocatalysts [54]. As illustrated in Fig. 3c, the EIS spectra display that the $Ni@NiS_x$ -CdS sample has a smaller arc radius of the Nyquist plot compared to the other samples, indicating the minimization of the charge transfer barrier and superior charge transport kinetics. This is ascribed to the fact that loading amorphous $Ni@NiS_x$ cocatalyst contribute to the electron transfer between the $Ni@NiS_x$ -CdS and electrolyte interface. The critical role of $Ni@NiS_x$ in improving the carrier migration efficiency can be demonstrated by the linear sweep voltammetry (LSV) curves. As shown in Fig. 3d, the LSV results show that the $Ni@NiS_x$ -CdS photocatalyst possesses lower H_2 evolution overpotential, which can convert water to H_2 evolution more efficiently [55]. Furthermore, the electrochemically active surface area (ECSA) of the as-synthesized photocatalysts were also investigated. The ECSA of the photocatalysts was compared by electrochemical double layer capacitance (C_{dl}) measurement [56]. As displayed in Fig. 3e and Fig. S7, the C_{dl} value of $Ni@NiS_x$ -CdS ($5.92 \text{ mF}\cdot\text{cm}^{-2}$) is higher than that of CdS ($1.64 \text{ mF}\cdot\text{cm}^{-2}$) and NiS_x -CdS ($3.69 \text{ mF}\cdot\text{cm}^{-2}$), which implies that $Ni@NiS_x$ -CdS has the larger active surface area.

Photoluminescence (PL) and time-resolved PL (TRPL) are powerful means to study the dynamics of photogenerated carriers. As given in

Fig. 3f, the PL spectrum was tested with an excitation wavelength of 325 nm. An intense emission peak was detected for CdS due to the rapid recombination of the charge carriers. Notably, the PL spectra showed a significant quenching of the fluorescence signal in $Ni@NiS_x$ -CdS compared to CdS and NiS_x -CdS photocatalysts, revealing efficient separation of photogenerated charge carriers. In addition, the lifetimes of free carriers in photocatalysts were probed by time-resolved fluorescence decay curves in Fig. 3g and Table S5. The $Ni@NiS_x$ -CdS sample has a longer average fluorescence lifetime ($\tau_{ave}=4.39 \text{ ns}$) compared with CdS ($\tau_{ave}=3.22 \text{ ns}$) and NiS_x -CdS ($\tau_{ave}=3.98 \text{ ns}$), stating that $Ni@NiS_x$ act as a cocatalyst to retard the recombination of charge carriers. The surface photovoltage (SPV) spectra is an effective technique to monitor the transfer path of photo-induced charge carriers in Fig. 3h. Noticeably, $Ni@NiS_x$ -CdS exhibits the lowest SPV intensity, which stems from the fact that the wrapping of $Ni@NiS_x$ can alter the migration pathway of photo-induced charge carriers. Since the $Ni@NiS_x$ is wrapped on the surface of the CdS, more photogenerated electrons accumulate on the surface of the $Ni@NiS_x$, which can counteract the positive photoelectric signal, thus leading to a decrease in the SPV signal of the $Ni@NiS_x$ -CdS [57]. The lowest SPV signal of $Ni@NiS_x$ -CdS indicates the effective separation and transfer of photogenerated charge carriers, ensuring maximum utilization of photogenerated charge carriers. Electron spin resonance (ESR) was employed to detect the signal intensity of superoxide radicals ($\cdot O_2^-$) and hydroxyl radicals ($\cdot OH$) using 5,5-dimethyl-1-pyrroline N-oxide (DMPO) as a trapping reagent (Fig. 3i and Fig. S8). The ESR signal could not be observed under dark conditions. However, CdS,

NiS_x-CdS and Ni@NiS_x-CdS showed various signal intensities after 10 min irradiation, indicating the presence of effective photogenerated electron-hole pairs. Notably, Ni@NiS_x-CdS exhibited stronger DMPO-·O₂ signal and DMPO-·OH signal than pristine CdS and NiS_x-CdS under irradiation for 10 min, which demonstrated that Ni@NiS_x-CdS possessed enhanced ability to separate charge carriers to generate the largest number of photogenerated electrons, thus boosting the H₂ evolution performance.

To further enlighten the origin of the superior photocatalytic H₂ production activity of Ni@NiS_x as cocatalyst, the density of states (DOS), Bader charge and charge density difference of NiS_x-CdS and Ni@NiS_x-CdS based on density functional theory (DFT) calculations and ab initio molecular dynamics (AIMD) simulations were performed. A typical Ni@NiS_x-CdS model was built, including Ni nanoclusters encapsulated into amorphous NiS_x to form a cocatalyst deposited on the CdS (002) surface, meanwhile the theoretical model of the NiS_x-CdS was constructed by loading amorphous NiS_x on the CdS (002) surface. The electron density at the Fermi energy level significantly dominates the

catalytic reaction [58]. As indicated in Fig. 4a-c, the electron density of Ni@NiS_x-CdS at the Fermi energy level is higher than that of NiS_x-CdS and CdS, which demonstrates the enhanced charge transport capacity of Ni@NiS_x-CdS compared to NiS_x-CdS and CdS, thus leading to the improved photocatalytic activity of the Ni@NiS_x-CdS photocatalyst. As displayed in Fig. 4d-f, the work functions (Φ) of CdS, NiS_x, and Ni clusters are calculated to be 4.64, 5.27, and 5.32 eV, respectively. The gradient work function variation provides the driving force to promote the flow of photogenerated electrons along the interface of Ni@NiS_x-CdS, which can be evidenced by charge density difference. As shown in Fig. 4g and j, the charge redistribution at the amorphous-crystalline interface verifies the massive electrons transfer across the amorphous-crystalline interface. Moreover, 3D charge density difference indicates that there is more pronounced electron accumulation on Ni@NiS_x cocatalyst than that of NiS_x, indicating stronger electron coupling effect at the Ni@NiS_x-CdS interface, which is more favorable for electron transfer from CdS to Ni@NiS_x with the aid of Cd-S-Ni bond bridge. Benefiting from the interfacial electronic coupling

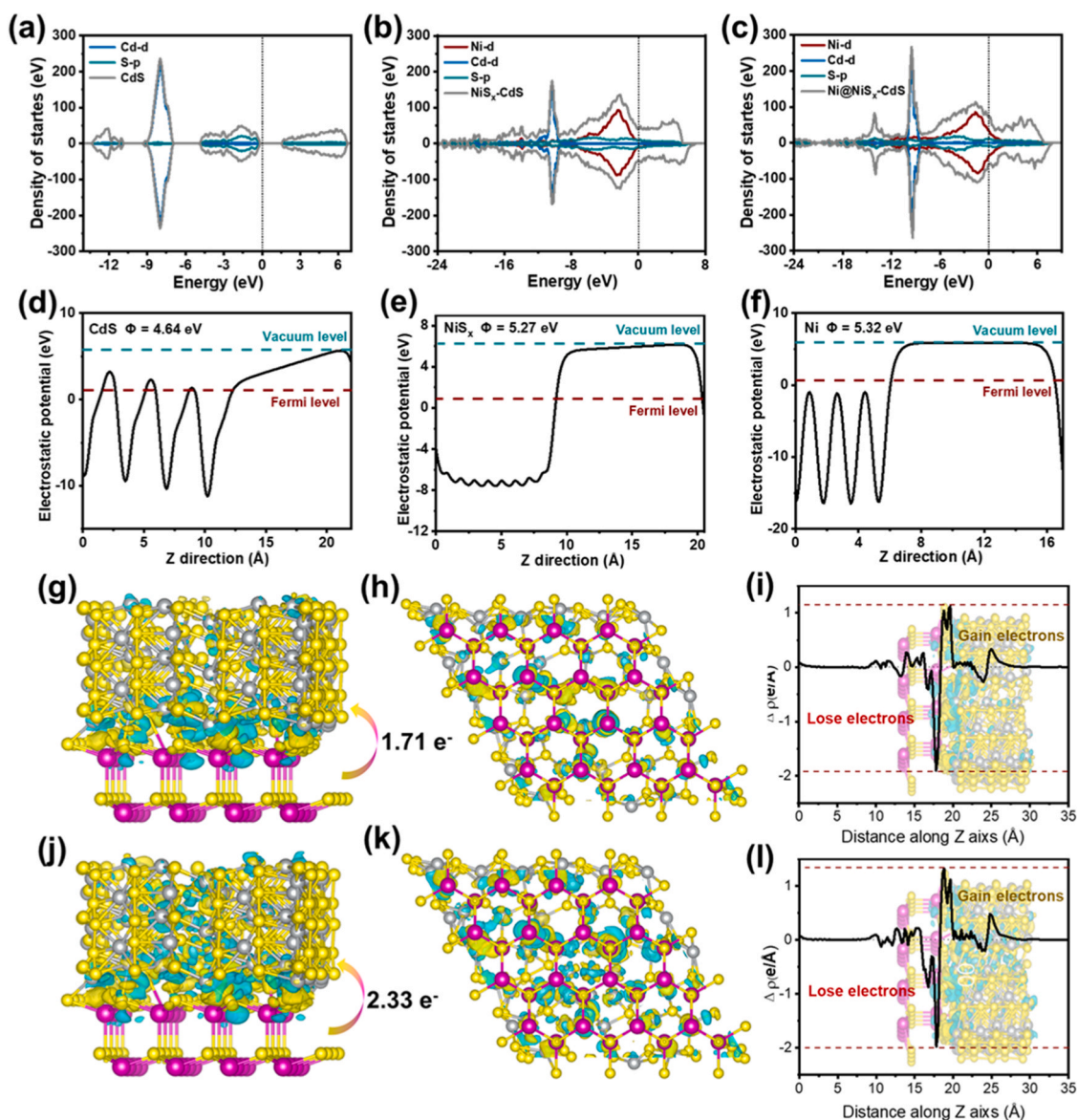


Fig. 4. Total DOS and PDOS of (a) CdS, (b) NiS_x-CdS and (c) Ni@NiS_x-CdS. Electrostatic potential of (d) CdS, (e) NiS_x and (f) Ni clusters. Side and top views of charge density difference and planar-averaged electron density difference along with Z-direction of Ni@NiS_x-CdS (g-i) and NiS_x-CdS photocatalyst (j-l). The green and yellow areas indicate the loss and accumulation of electrons, respectively. The positive and negative values of $\Delta\rho$ represent the accumulation and consumption of electrons, respectively.

effect and chemical bond, the transferred Bader charges from CdS to NiS_x is 1.17 e⁻. Notably, the Bader charges of Ni@NiS_x from CdS is calculated as 2.33 e⁻, which is higher than that of NiS_x from CdS, suggesting that the embedding of Ni clusters in the amorphous NiS_x enhance electron extraction capability of the Ni@NiS_x cocatalyst. The above electron transfer is further supported by the planar average charge density difference along the Z-direction (Fig. 4i and l), which intuitively presents the variation of the charge density distribution and agrees with the shift trend of XPS and theoretical work function. These results imply that more available electrons in Ni@NiS_x -CdS can be devoted to the surface photocatalytic reduction reaction.

The reconfigured electronic structure of the active sites on the composite photocatalyst is deemed to favor for the adsorption and

activation of H_2O molecules and the modulation of H^* adsorption free energies (ΔG_{H^*}), thus leading to boosted photocatalytic H_2 reaction reactivity. The optimized structural configurations of H_2O adsorption energy and H^* adsorption free energy (ΔG_{H^*}) at various sites of NiS_x -CdS and Ni@NiS_x -CdS were presented (Fig. 5a and c). The adsorption of H_2O molecules is the preliminary step of the photocatalytic H_2O splitting process, which is essential for the enhancement of alkaline photocatalytic H_2 production [59]. As displayed in Fig. 5b, the Ni site in Ni@NiS_x hold a much lower H_2O molecular adsorption energy (-1.88 eV) than the other three sites, which demonstrate that the Ni site in Ni@NiS_x is more favorable for H_2O adsorption. As a result, the length of the O-H bond in H_2O molecules was prolonged 1.11 Å on the Ni site in Ni@NiS_x -CdS (Table S6). In addition, the H_2O molecule was bent at an

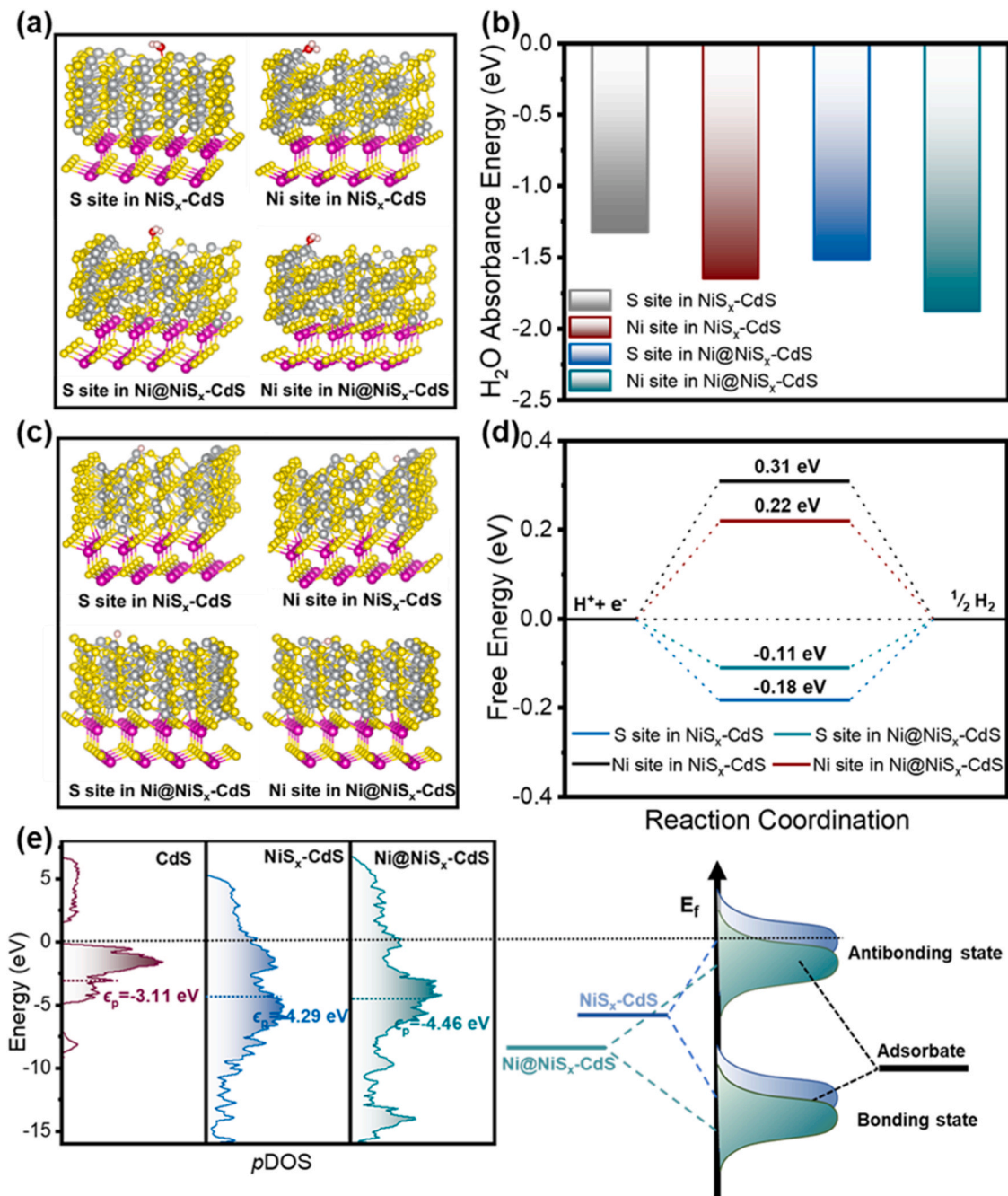


Fig. 5. (a) Optimized H_2O molecular adsorption configurations and (b) calculated adsorption energy of H_2O . (c) Optimized structural configurations of H^* adsorbed Gibbs free energy and (d) Gibbs free energy (ΔG_{H^*}) diagram of the Ni and S site of Ni@NiS_x -CdS and NiS_x -CdS, respectively. (e) p-band centers for CdS, NiS_x -CdS and Ni@NiS_x -CdS and the corresponding schematic illustration of bond formation between the photocatalyst surface and the adsorbate.

even larger angle of 109.48° , which indicated that enhanced adsorption and activation of H_2O molecule on the Ni site in $\text{Ni@NiS}_x\text{-CdS}$ would further promote the dissociation of H_2O [60]. More importantly, the value of the Gibbs free energy of the H^* adsorption (ΔG_{H^*}) is closely correlated with the H_2 evolution activity, where the closer the value of ΔG_{H^*} approaches to 0 eV, the more favorable is the desorption of H^* intermediate and rapid H_2 generation kinetics [61]. As revealed in Fig. 5d, the ΔG_{H^*} on the active S sites in $\text{Ni@NiS}_x\text{-CdS}$ was calculated to be -0.11 eV, followed by S sites of $\text{NiS}_x\text{-CdS}$ (-0.18 eV), Ni sites of $\text{Ni@NiS}_x\text{-CdS}$ (0.22 eV), and Ni sites of $\text{NiS}_x\text{-CdS}$ (0.31 eV). The absolute value of the ΔG_{H^*} on the S site in $\text{Ni@NiS}_x\text{-CdS}$ is smaller than that of $\text{NiS}_x\text{-CdS}$, confirming that the S site in Ni@NiS_x act as the more energetically active site for photocatalytic H_2 evolution. DFT calculations support the experimental results, indicating that the electronic coupling at the interface and the encapsulation of Ni clusters synergically modulate the electronic structures of S sites, activate the activity of the active S sites in Ni@NiS_x , and decline Gibbs free energy barrier (ΔG_{H^*}) of H_2 evolution reaction, which is consistent with the remarkably improved photocatalytic activity of $\text{Ni@NiS}_x\text{-CdS}$ photocatalyst. It is well known that the location of the S p-band center is an essential indicator for the adsorption of H^* intermediate, reflecting H_2 evolution activity. Thus, the partial density of states (pDOS) and the S p-band center are calculated. As displayed in Fig. 5e, the calculated the S p-band centers in CdS, $\text{NiS}_x\text{-CdS}$ and $\text{Ni@NiS}_x\text{-CdS}$ are located at -3.11 , -4.29 , and -4.46 eV, respectively. The S p-band center in CdS is closest to the Fermi energy level, indicating that it has a strong H^* intermediate adsorption energy, which is adverse for rapid desorption of H_2 , thus resulting in a sluggish photocatalytic reduction kinetics. The downward shift of the S p-band center in $\text{NiS}_x\text{-CdS}$ demonstrates that the strong electronic coupling of amorphous-crystalline $\text{NiS}_x\text{-CdS}$ interface contribute to weakening the H^* intermediate adsorption. For $\text{Ni@NiS}_x\text{-CdS}$, the embedded Ni clusters is advantageous for charge extraction at the $\text{Ni@NiS}_x\text{-CdS}$ photocatalyst, which achieved a further downward shift of the S p-band center from the Fermi level, facilitating the H^* intermediate desorption from active S sites for enhanced H_2 evolution reaction. As shown in the Fig. 5e, the antibonding states of S sites increase with the downward shift of the p-band center, and the interaction between the adsorbate H^* intermediate and the active S site is weakened, which conforms to the ΔG_{H^*} calculation.

4. Conclusion

In summary, an amorphous Ni@NiS_x cocatalyst has been successfully assembled on the crystalline CdS surface via the facile partial reduction strategy. Benefitting from the structural and compositional merits, the as-synthesized $\text{Ni@NiS}_x\text{-CdS}$ sample exhibit superior photocatalytic performance with the H_2 production rate of $78.7 \text{ mmol}\cdot\text{g}^{-1}\cdot\text{h}^{-1}$ under visible light irradiation, which is 18.3 and 1.5 times higher than that of CdS and $\text{NiS}_x\text{-CdS}$, respectively, surpassing the majority of the reported CdS-based photocatalysts. Besides, the optimal $\text{Ni@NiS}_x\text{-CdS}$ photocatalyst achieves a high quantum efficiency of 36.74% at 420 nm and presents favorable photostability and reusability. Experimental characterizations combined with DFT calculations confirm that the synergistic effects between the interfacial charge transfer of the amorphous-crystalline $\text{Ni@NiS}_x\text{-CdS}$ photocatalyst and the gradient work function variation induced by encapsulation of Ni clusters into amorphous NiS_x layer not only tailors the S p-band center away from Fermi level in $\text{Ni@NiS}_x\text{-CdS}$ photocatalyst to optimize the Gibbs free energy of atomic H_2 adsorption, but also boosts charge extraction ability to inhibit carrier recombination. In addition, the amorphous NiS_x layer exposes abundant unsaturated S sites, thereby capturing both protons and electrons. This work provides a unique strategy for establishing nanocomposite cocatalyst coupled semiconductor to enhance high-efficiently photocatalytic water splitting performance.

CRediT authorship contribution statement

Xinlei Zhang: Investigation, Methodology, Writing – original draft. **Fei Wu:** Investigation, Data curation. **Guicun Li:** Validation. **Lei Wang:** Validation. **Jianfeng Huang:** Formal analysis. **Alan Meng:** Writing – review & editing. **Zhenjiang Li:** Supervision, Writing – review & editing. All authors have approved the final version of the manuscript.

Declaration of Competing Interest

The authors declare that they have no known competing financial interests or personal relationships that could have appeared to influence the work reported in this paper.

Data availability

Data will be made available on request.

Acknowledgements

The work reported here was supported by the National Natural Science Foundation of China under Grant No. 52072196, 52002199, 52002200, 52102106, Major Basic Research Program of Natural Science Foundation of Shandong Province under Grant No. ZR2020ZD09, the Natural Science Foundation of Shandong Province under Grant No. ZR2019BEM042, ZR2020QE063, the Innovation and Technology Program of Shandong Province under Grant No. 2020KJA004, the Taishan Scholar Project of Shandong Province under No. ts201511034. We express our grateful thanks to them for their financial support.

Appendix A. Supporting information

Supplementary data associated with this article can be found in the online version at doi:10.1016/j.apcatb.2023.123398.

References

- [1] Q. Wang, K. Domen, Particulate photocatalysts for light-driven water splitting: mechanisms, challenges, and design strategies, *Chem. Rev.* 120 (2020) 919–985.
- [2] X.-B. Li, Z.-K. Xin, S.-G. Xia, X.-Y. Gao, C.-H. Tung, L.-Z. Wu, Semiconductor nanocrystals for small molecule activation via artificial photosynthesis, *Chem. Soc. Rev.* 49 (2020) 9028–9056.
- [3] C. Feng, Z.P. Wu, K.W. Huang, J. Ye, H. Zhang, Surface modification of 2D photocatalysts for solar energy conversion, *Adv. Mater.* 34 (2022), 2200180.
- [4] C. Cheng, B. He, J. Fan, B. Cheng, S. Cao, J. Yu, An inorganic/organic S-scheme heterojunction h_2 -production photocatalyst and its charge transfer mechanism, *Adv. Mater.* 33 (2021), 2100317.
- [5] Z. Li, W. Huang, J. Liu, K. Lv, Q. Li, Embedding CdS@Au into ultrathin $\text{Ti}_{3-x}\text{C}_2\text{T}_y$ to build dual schottky barriers for photocatalytic H_2 production, *ACS Catal.* 11 (2021) 8510–8520.
- [6] J. Ran, H. Zhang, S. Fu, M. Jaroniec, J. Shan, B. Xia, Y. Qu, J. Qu, S. Chen, L. Song, J.M. Cairney, L. Jing, S.-Z. Qiao, NiPS₃ ultrathin nanosheets as versatile platform advancing highly active photocatalytic H_2 production, *Nat. Commun.* 13 (2022), 4600.
- [7] Y. Wu, X. Chen, J. Cao, Y. Zhu, W. Yuan, Z. Hu, Z. Ao, G.W. Brudvig, F. Tian, J. C. Yu, C. Li, Photocatalytically recovering hydrogen energy from wastewater treatment using $\text{MoS}_2/\text{TiO}_2$ with sulfur/oxygen dual-defect, *Appl. Catal. B: Environ.* 303 (2022), 120878.
- [8] Y. Kageshima, T. Kawanishi, D. Saeki, K. Teshima, K. Domen, H. Nishikiori, Boosted hydrogen-evolution kinetics over particulate lanthanum and rhodium-doped strontium titanate photocatalysts modified with phosphonate groups, *Angew. Chem. Int. Ed.* 60 (2021) 3654–3660.
- [9] X. Chen, J. Wang, Y. Chai, Z. Zhang, Y. Zhu, Efficient photocatalytic overall water splitting induced by the giant internal electric field of a $\text{g-C}_3\text{N}_4/\text{rGO}/\text{PDIP}$ Z-scheme heterojunction, *Adv. Mater.* 33 (2021), 2007479.
- [10] J. Li, A. Slassi, X. Han, D. Cornil, M.-H. Ha-Thi, T. Pino, D.P. Debecker, C. Colbeau-Justin, J. Arbiol, J. Cornil, M.N. Ghazzal, Tuning the electronic bandgap of graphdiyne by H-substitution to promote interfacial charge carrier separation for enhanced photocatalytic hydrogen production, *Adv. Funct. Mater.* 31 (2021), 2100994.
- [11] M. Zhao, S. Liu, D. Chen, S. Zhang, S.N.A.C. Carabineiro, K. Lv, A novel S-scheme 3D $\text{ZnIn}_2\text{S}_4/\text{WO}_3$ heterostructure for improved hydrogen production under visible light irradiation, *Chin. J. Catal.* 43 (2022) 2615–2624.

- [12] Z. Qi, J. Chen, Q. Li, N. Wang, Sn.A.C. Carabineiro, K. Lv, Increasing the photocatalytic hydrogen generation activity of CdS nanorods by introducing interfacial and polarization electric fields, *Small* N./a (2023), 2303318.
- [13] X. Xiao, Y. Gao, L. Zhang, J. Zhang, Q. Zhang, Q. Li, H. Bao, J. Zhou, S. Miao, N. Chen, J. Wang, B. Jiang, C. Tian, H. Fu, A promoted charge separation/transfer system from Cu single atoms and C_3N_4 layers for efficient photocatalysis, *Adv. Mater.* 32 (2020), 2003082.
- [14] S. Hejazi, S. Mohajernia, B. Osuagwu, G. Zoppellaro, P. Andryskova, O. Tomanec, S. Kment, R. Zboril, P. Schmuki, On the controlled loading of single platinum atoms as a Co-catalyst on TiO_2 anatase for optimized photocatalytic H_2 generation, *Adv. Mater.* 32 (2020), 1908505.
- [15] K. Li, S. Zhang, Y. Li, J. Fan, K. Lv, MXenes as noble-metal-alternative co-catalysts in photocatalysis, *Chin. J. Catal.* 42 (2021) 3–14.
- [16] Y. Goto, K.-i. Yamanaka, M. Ohashi, Y. Maegawa, S. Inagaki, Light-harvesting photocatalysis for H_2 evolution by methylacridone-bridged periodic mesoporous organosilica, *Appl. Catal. B: Environ.* 287 (2021), 119965.
- [17] Z. Lin, Y. Zhao, J. Luo, S. Jiang, C. Sun, S. Song, Apparent potential difference boosting directional electron transfer for full solar spectrum-irradiated catalytic H_2 evolution, *Adv. Funct. Mater.* 30 (2020), 1908797.
- [18] Y. Chao, J. Zheng, H. Zhang, F. Li, F. Yan, Y. Tan, Z. Zhu, Oxygen-incorporation in Co_2P as a non-noble metal cocatalyst to enhance photocatalysis for reducing water to H_2 under visible light, *Chem. Eng. J.* 346 (2018) 281–288.
- [19] Y. Liu, Y.-H. Li, X. Li, Q. Zhang, H. Yu, X. Peng, F. Peng, Regulating electron-hole separation to promote photocatalytic H_2 evolution activity of nanoconfined Ru/MXene/ TiO_2 catalysts, *ACS Nano* 14 (2020) 14181–14189.
- [20] Y. Li, S. Wang, P. Wang, Y. He, X. Wang, K. Chang, H. Lin, X. Ding, H. Chen, H. Zhang, Y. Izumi, T. Kako, J. Ye, Targeted removal of interfacial adventitious carbon towards directional charge delivery to isolated metal sites for efficient photocatalytic H_2 production, *Nano Energy* 76 (2020), 105077.
- [21] H. Peng, T. Yang, H. Lin, Y. Xu, Z. Wang, Q. Zhang, S. Liu, H. Geng, L. Gu, C. Wang, X. Fan, W. Chen, X. Huang, Ru/In dual-single atoms modulated charge separation for significantly accelerated photocatalytic H_2 evolution in pure water, *Adv. Energy Mater.* 12 (2022), 2201688.
- [22] Y. Wu, Q. Wu, Q. Zhang, Z. Lou, K. Liu, Y. Ma, Z. Wang, Z. Zheng, H. Cheng, Y. Liu, Y. Dai, B. Huang, P. Wang, An organometal halide perovskite supported Pt single-atom photocatalyst for H_2 evolution, *Energy Environ. Sci.* 15 (2022) 1271–1281.
- [23] H. Yao, X. Wang, K. Li, C. Li, C. Zhang, J. Zhou, Z. Cao, H. Wang, M. Gu, M. Huang, H. Jiang, Strong electronic coupling between ruthenium single atoms and ultrafine nanoclusters enables economical and effective hydrogen production, *Appl. Catal. B: Environ.* 312 (2022), 121378.
- [24] S. Yuan, Z. Pu, H. Zhou, J. Yu, I.S. Amiin, J. Zhu, Q. Liang, J. Yang, D. He, Z. Hu, G. Van Tendeloo, S. Mu, A universal synthesis strategy for single atom dispersed cobalt/metal clusters heterostructure boosting hydrogen evolution catalysis at all pH values, *Nano Energy* 59 (2019) 472–480.
- [25] Z. Pu, I.S. Amiin, R. Cheng, P. Wang, C. Zhang, S. Mu, W. Zhao, F. Su, G. Zhang, S. Liao, S. Sun, Single-atom catalysts for electrochemical hydrogen evolution reaction: recent advances and future perspectives, *Nano-Micro Lett.* 12 (2020), 21.
- [26] B. He, C. Bie, X. Fei, B. Cheng, J. Yu, W. Ho, A.A. Al-Ghamdi, S. Wageh, Enhancement in the photocatalytic H_2 production activity of CdS NRs by Ag_2S and NiS dual cocatalysts, *Appl. Catal. B: Environ.* 288 (2021), 119994.
- [27] K. Li, H. Pan, F. Wang, Z. Zhang, S. Min, In-situ exsolved NiS nanoparticle-socketed CdS with strongly coupled interfaces as a superior visible-light-driven photocatalyst for hydrogen evolution, *Appl. Catal. B: Environ.* 321 (2023), 122028.
- [28] J. Zhang, L. Qi, J. Ran, J. Yu, S.Z. Qiao, Ternary $Ni_3S_2/Zn_3Cd_{1-x}S$ /reduced graphene oxide nanocomposites for enhanced solar photocatalytic H_2 -production activity, *Adv. Energy Mater.* 4 (2014), 1301925.
- [29] W. Zhong, X. Wu, Y. Liu, X. Wang, J. Fan, H. Yu, Simultaneous realization of sulfur-rich surface and amorphous nanocluster of NiS_{1+x} cocatalyst for efficient photocatalytic H_2 evolution, *Appl. Catal. B: Environ.* 280 (2021), 119455.
- [30] P. Wang, S. Xu, F. Chen, H. Yu, Ni nanoparticles as electron-transfer mediators and NiS_x as interfacial active sites for coordinative enhancement of H_2 -evolution performance of TiO_2 , *Chin. J. Catal.* 40 (2019) 343–351.
- [31] Y. Zhang, W. Zhou, Y. Tang, Y. Guo, Z. Geng, L. Liu, X. Tan, H. Wang, T. Yu, J. Ye, Unravelling unsaturated edge S in amorphous NiS_x for boosting photocatalytic H_2 evolution of metastable phase CdS confined inside hydrophilic beads, *Appl. Catal. B: Environ.* 305 (2022), 121055.
- [32] G. Zhou, Z. Zhou, Y. Xia, W. Yin, J. Hou, X. Zhu, J. Yi, S. Wang, X. Ning, X. Wang, Synchronous synthesis of S-doped carbon nitride/nickel sulfide photocatalysts for efficient dye degradation and hydrogen evolution, *Appl. Surf. Sci.* 608 (2023), 154974.
- [33] Z. Wang, X. Mou, D. Li, C. Song, D. Wang, Hierarchical flower-like amorphous nickel sulfide/crystalline CoFe layered double hydroxide heterostructure for overall water splitting, *Int. J. Hydrog. Energy* (2022).
- [34] W. Zhong, D. Gao, H. Yu, J. Fan, J. Yu, Novel amorphous $NiCuS_x$ H_2 -evolution cocatalyst: optimizing surface hydrogen desorption for efficient photocatalytic activity, *Chem. Eng. J.* 419 (2021), 129652.
- [35] D. Gao, B. Zhao, L. Wang, E. Aslan, I. Hatay Patir, J. Yu, H. Yu, Electron-enriched regulation of sulfur-active site for accelerating atomic hydrogen desorption of S-rich $MoWS_{2+x}$ cocatalyst toward efficient photocatalytic H_2 evolution of TiO_2 , *Chem. Eng. J.* 449 (2022), 137803.
- [36] X.-Y. Zhou, J.-L. Zhou, R. Guo, Y.-j. Liu, Y.-f. Yu, B. Zhang, Y.-W. Wu, L. Zhao, Q. Lu, Effect of flue gas components on the removal of cadmium pollutants by transition metal-modified activated carbon: density functional theory and thermodynamic study, *Fuel* 343 (2023), 128011.
- [37] Y. Liu, J. Wu, K.P. Hackenberg, J. Zhang, Y.M. Wang, Y. Yang, K. Keyshar, J. Gu, T. Ogitsu, R. Vajtai, J. Lou, P.M. Ajayan, B.C. Wood, B.I. Yakobson, Self-optimizing, highly surface-active layered metal dichalcogenide catalysts for hydrogen evolution, *Nat. Energy* 2 (2017), 17127.
- [38] L. Zhu, H. Lin, Y. Li, F. Liao, Y. Lifshitz, M. Sheng, S.-T. Lee, M. Shao, A rhodium/silicon co-electrocatalyst design concept to surpass platinum hydrogen evolution activity at high overpotentials, *Nat. Commun.* 7 (2016), 12272.
- [39] J. He, W. Zhong, Y. Xu, H. Yu, J. Fan, J. Yu, Few-layered $Mo_xW_{1-x}S_2$ -modified CdS photocatalyst: one-step synthesis with bifunctional precursors and improved H_2 -evolution activity, *Sol. RRL* 5 (2021), 2100387.
- [40] W. Zhong, D. Gao, P. Wang, X. Wang, H. Yu, Accelerating hydroxyl desorption by swapping catalytic sites in $RuMoS_{2+x}$ cocatalysts for efficient alkaline photocatalytic H_2 production, *Appl. Catal. B: Environ.* 319 (2022), 121910.
- [41] Y. Wang, X. Li, Z. Huang, H. Wang, Z. Chen, J. Zhang, X. Zheng, Y. Deng, W. Hu, Amorphous Mo-doped $NiS_{0.5}Se_{0.5}$ nanosheets/crystalline $NiS_{0.5}Se_{0.5}$ nanorods for high current-density electrocatalytic water splitting in neutral media, *Angew. Chem. Int. Ed.* 62 (2023) 202215256.
- [42] S. Shen, Z. Wang, Z. Lin, K. Song, Q. Zhang, F. Meng, L. Gu, W. Zhong, Crystalline-amorphous interfaces coupling of $CoSe_2/CoP$ with optimized d-band center and boosted electrocatalytic hydrogen evolution, *Adv. Mater.* 34 (2022), 2110631.
- [43] Y. Tang, X. Jia, Y. Guo, Z. Geng, C. Wang, L. Liu, J. Zhang, W. Guo, X. Tan, T. Yu, J. Ye, Surface unsaturated sulfur modulates Pt Sub-Nanoparticles on Tandem Homo Junction CdS for efficient electron extraction, *Adv. Energy Mater.* 13 (2023), 2203827.
- [44] D. Gao, H. Long, X. Wang, J. Yu, H. Yu, Tailoring antibonding-orbital occupancy state of selenium in Se-enriched $ReSe_{2+x}$ cocatalyst for exceptional H_2 evolution of TiO_2 photocatalyst, *Adv. Funct. Mater.* 33 (2023), 2209994.
- [45] D. Gao, J. Xu, L. Wang, B. Zhu, H. Yu, J. Yu, Optimizing atomic hydrogen desorption of sulfur-rich NiS_{1+x} cocatalyst for boosting photocatalytic H_2 evolution, *Adv. Mater.* 34 (2022), 2108475.
- [46] G. Liu, C. Kolodziej, R. Jin, S. Qi, Y. Lou, J. Chen, D. Jiang, Y. Zhao, C. Burda, MoS_2 -stratified $CdS-Cu_{2-x}S$ core-shell nanorods for highly efficient photocatalytic hydrogen production, *ACS Nano* 14 (2020) 5468–5479.
- [47] Y. Liu, S. Ding, Y. Shi, X. Liu, Z. Wu, Q. Jiang, T. Zhou, N. Liu, J. Hu, Construction of CdS/CoO_x core-shell nanorods for efficient photocatalytic H_2 evolution, *Appl. Catal. B: Environ.* 234 (2018) 109–116.
- [48] X. Xue, W. Dong, Q. Luan, H. Gao, G. Wang, Novel interfacial lateral electron migration pathway formed by constructing metallized CoP_2/CdS interface for excellent photocatalytic hydrogen production, *Appl. Catal. B: Environ.* 334 (2023), 122860.
- [49] Z. Lei, X. Cao, J. Fan, X. Hu, J. Hu, N. Li, T. Sun, E. Liu, Efficient photocatalytic H_2 generation over $In_{2.77}S_4/NiS_2/g-C_3N_4$ S-scheme heterojunction using NiS_2 as electron-bridge, *Chem. Eng. J.* 457 (2023), 141249.
- [50] X. Yu, X. Ren, Z. Yuan, X. Hou, T. Yang, M. Wang, Ni_3S_2-Ni hybrid nanospheres with intra-core void structure encapsulated in N-doped carbon shells for efficient and stable K-ion storage, *Adv. Sci.* 10 (2023), 2205556.
- [51] P. Zhang, L.-j. Wu, W.-g. Pan, S.-c. Bai, R.-t. Guo, Efficient photocatalytic H_2 evolution over $NiS-PCN$ Z-scheme composites via dual charge transfer pathways, *Appl. Catal. B: Environ.* 289 (2021), 120040.
- [52] S. Zhang, Y. Liu, R. Ma, D. Jia, T. Wen, Y. Ai, G. Zhao, F. Fang, B. Hu, X. Wang, Molybdenum (VI)-oxo clusters incorporation activates $g-C_3N_4$ with simultaneously regulating charge transfer and reaction centers for boosting photocatalytic performance, *Adv. Funct. Mater.* 32 (2022), 2204175.
- [53] Y. Guo, L. Mao, Y. Tang, Q. Shang, X. Cai, J. Zhang, H. Hu, X. Tan, L. Liu, H. Wang, T. Yu, J. Ye, Concentrating electron and activating H-OH bond of absorbed water on metallic $NiCo_2S_4$ boosting photocatalytic hydrogen evolution, *Nano Energy* 95 (2022), 107028.
- [54] B. Dai, J. Fang, Y. Yu, M. Sun, H. Huang, C. Lu, J. Kou, Y. Zhao, Z. Xu, Construction of infrared-light-responsive photoinduced carriers driver for enhanced photocatalytic hydrogen evolution, *Adv. Mater.* 32 (2020), 1906361.
- [55] C. Wu, W. Huang, H. Liu, K. Lv, Q. Li, Insight into synergistic effect of Ti_3C_2 MXene and MoS_2 on anti-photocorrosion and photocatalytic of CdS for hydrogen production, *Appl. Catal. B: Environ.* 330 (2023), 122653.
- [56] G. Peng, L. Xing, J. Barrio, M. Volokh, M. Shalom, A general synthesis of porous carbon nitride films with tunable surface area and photophysical properties, *Angew. Chem. Int. Ed.* 57 (2018) 1186–1192.
- [57] X. Li, S. Song, Y. Gao, L. Ge, W. Song, T. Ma, J. Liu, Identification of the charge transfer channel in cobalt encapsulated hollow nitrogen-doped carbon matrix@CdS heterostructure for photocatalytic hydrogen evolution, *Small* 17 (2021), 2101315.
- [58] H. Gu, H. Zhang, X. Wang, Q. Li, S. Chang, Y. Huang, L. Gao, Y. Cui, R. Liu, W.-L. Dai, Robust construction of CdSe nanorods/ Ti_3C_2 MXene nanosheet for superior photocatalytic H_2 evolution, *Appl. Catal. B: Environ.* 328 (2023), 122537.
- [59] P. Wang, T. Wang, R. Qin, Z. Pu, C. Zhang, J. Zhu, D. Chen, D. Feng, Z. Kou, S. Mu, J. Wang, Swapping catalytic active sites from cationic Ni to anionic S in nickel sulfide enables more efficient alkaline hydrogen generation, *Adv. Energy Mater.* 12 (2022), 2103359.
- [60] M. Zhou, H. Li, A. Long, B. Zhou, F. Lu, F. Zhang, F. Zhan, Z. Zhang, W. Xie, X. Zeng, D. Yi, X. Wang, Modulating 3d orbitals of Ni atoms on Ni-Pt edge sites enables highly-efficient alkaline hydrogen evolution, *Adv. Energy Mater.* 11 (2021), 2101789.
- [61] R. Zhao, Y. Wang, G. Ji, J. Zhong, F. Zhang, M. Chen, S. Tong, P. Wang, Z. Wu, B. Han, Z. Liu, Partially nitrated Ni nanoclusters achieve energy-efficient electrocatalytic CO_2 reduction to CO at ultralow overpotential, *Adv. Mater.* 35 (2022), 2205262.
- [62] G. Zhang, D. Chen, N. Li, Q. Xu, H. Li, J. He, J. Lu, Preparation of $ZnIn_2S_4$ nanosheet-coated CdS nanorod heterostructures for efficient photocatalytic reduction of $Cr(VI)$, *Appl. Catal. B: Environ.* 232 (2018) 164–174.